

# Topological photonic crystal fibre

Bofeng Zhu\*,<sup>1,2</sup> Kevin Hean\*,<sup>2</sup> Stephan Wong,<sup>3</sup> Yuxi Wang,<sup>2</sup> Rimi Banerjee,<sup>1</sup> Haoran Xue,<sup>4</sup>  
Qiang Wang,<sup>5</sup> Alexander Cerjan,<sup>3</sup> Qi Jie Wang,<sup>1,2,6</sup> Wonkeun Chang,<sup>2</sup> and Y. D. Chong<sup>1,6</sup>

<sup>1</sup>*Division of Physics and Applied Physics,*

*School of Physical and Mathematical Sciences,*

*Nanyang Technological University, Singapore 637371, Singapore*

<sup>2</sup>*School of Electrical and Electronic Engineering,*

*Nanyang Technological University, Singapore 637371, Singapore\**

<sup>3</sup>*Center for Integrated Nanotechnologies,*

*Sandia National Laboratories, Albuquerque, New Mexico 87185, USA*

<sup>4</sup>*Department of Physics,*

*The Chinese University of Hong Kong, Shatin, Hong Kong SAR, China*

<sup>5</sup>*Collaborative Innovation Center of Advanced Microstructures,*

*School of Physics, Nanjing University, Nanjing, Jiangsu 210093, China*

<sup>6</sup>*Centre for Disruptive Photonic Technologies,*

*Nanyang Technological University, Singapore 637371, Singapore<sup>†</sup>*

Photonic crystal fibres (PCFs) [1–8, 51] are optical fibres that guide light using a modulated dielectric medium [3, 4]. They provide an exceptionally versatile platform for various applications, thanks to the flexibility with which light-guiding can be customised by modifying the fibre geometry [3]. Here, we realise a PCF with guided modes produced by photonic bandstructure topology [9–11] rather than conventional mode-trapping mechanisms. The design, which is compatible with the stack-and-draw fabrication process, consists of a cross-sectional photonic topological crystalline insulator [11–13] with a disclination. A bulk-defect correspondence [14, 15] produces degenerate topological modes, lying below the cladding light line. We use various theoretical methods to confirm their topological origins, including a spectral localiser that makes minimal assumptions about the bandstructure [16–19]. Our experiments on the fabricated topological fibre show it transmitting visible to near-infrared light with low losses of 10–20 dB/km, which do not increase much when the fibre is bent. A comparable solid-core PCF of conventional design exhibits substantially higher bending losses. Optical fibres based on topological modes thus hold promise for improved performance and novel functionalities.

PCFs are a subset of the broader class of photonic crystals: structures that use wavelength-scale modulations to manipulate light [1, 21]. Photonic crystals have been used in efficient lasers [22] and solar cells [23], but arguably their most important applications involve PCFs, including high-power light delivery [5], supercontinuum light generation [24], and sensing [25]. In recent years, a new approach to designing photonic crystals, called topological photonics, has emerged [9–11]. This involves engineering photonic bandstructures similar to those found in topological phases of condensed matter, thereby giving rise to distinctive photonic modes that owe their existence to topological “correspondence principles” rather than conventional light-trapping mechanisms [9, 11]. Aside from providing new avenues for fundamental research into band topology, topological photonics holds promise for device applications due to the robustness of topological modes against certain forms of disorder. There is a substantial amount of ongoing research on topological waveguides [26, 27] and resonators [28–30], mostly based on the photonic crystal slab geometry, which is

---

\* These two authors contributed equally to this work.

† qjwang@ntu.edu.sg, wonkeun.chang@ntu.edu.sg, yidong@ntu.edu.sg

well-suited to photonic bandstructure engineering due to the availability of powerful fabrication techniques like photolithography. Bringing topological photonics into PCFs, however, has proven more challenging.

Previous theoretical proposals [31–34] for topological photonic crystal fibres have been hampered by incompatibility with existing fibre fabrication methods, reliance on materials that are hard to incorporate into fibres, or other difficulties. Numerous designs that have previously been explored in topological photonics, including those based on PhC slabs, seem to be incompatible with PCFs. Recently, researchers have developed a multicore PCF whose cores are placed in a Su-Schrieffer-Heeger configuration, a one-dimensional lattice with topological end-states [35]. However, that design is based on the arrangement of the waveguiding cores, not the topological properties of the underlying PCF’s bandstructure.

Here, we design and experimentally implement a topological photonic crystal fibre (TPCF) that guides light via robust topological modes, based on the concept of defect states in topological crystalline insulators (TCIs). Although studies of topological bandstructures usually focus on boundary states created by the bulk-boundary correspondence principle [9], lattice defects such as disclinations [36] can also host localised topological states due to the related bulk-defect correspondence principle [37], as shown in recent experiments [14, 15, 42]. Photonic defect modes based on other topological principles have also been demonstrated [38–41]. Specifically, TCIs—structures with nontrivial band topology sustained by lattice symmetries [11–13]—can host topological disclination states associated with fractionalised spectral charge, as shown recently in a pair of photonics-based experiments [14, 15]. Taking a similar approach, we design a TPCF whose two-dimensional (2D) cross section is a photonic TCI with a central disclination. The overall structure, consisting of glass capillaries and rods of different radii, is compatible with the standard stack-and-draw method for fabricating PCFs. The TCI hosts disclination states localised around a central air hole; when extruded along the fibre’s  $z$  axis, these form a set of ten waveguide modes that we call guided topological defect modes (GTDMs). To show that the GTDMs originate from nontrivial photonic band topology, we first establish that the underlying bulk TCI is topologically nontrivial and that the disclination traps fractional charges [14, 15]; then, we employ a recently-developed “spectral localiser” framework to specifically identify the GTDMs as topological states [16–19].

The GTDMs possess an unexpected feature that is advantageous for waveguiding: despite

originating from topological gaps in the bulk bandstructure, they do not reside in those gaps, nor in the bulk bands; instead, they lie below the lowest bulk band (i.e., below the cladding light line). This property, which is not disallowed by theoretical principles [12, 13], serves to inhibit cross-talk with the bulk states in a manner analogous to solid-core PCFs [6]. It allows for robust, broad-band waveguiding without a complete 3D bandgap of the sort employed in earlier demonstrations of guided defect modes (which used designs that are hard to implement in a PCF) [44, 45]. We experimentally measure the TPCF’s transmission loss to be 10–20 dB/km across much of the visible to near-infrared range. When the TPCF is strongly bent (2 loops of radius 1 cm), the measured output power decreases by less than 5 dBm throughout the operating frequency range, whereas a conventional solid-core PCF fabricated with the same equipment and facilities experiences a decrease of up to 25 dBm. The GTDMs also have an interesting structure that can be exploited for spatial and/or polarisation multiplexing. In the future, it will be interesting to see how such TPCFs, after appropriate performance optimisations, compare to state-of-the-art PCFs based on conventional design principles. Our work also points to optical fibres as an important platform for future work on topological photonics, with many unexplored application possibilities.

## 1. FIBRE DESIGN AND IMPLEMENTATION

The TPCF is translationally invariant along the fibre axis (denoted by  $z$ ), with a pattern of air holes in the transverse ( $x$ - $y$ ) plane (Fig. 1a). This cross sectional pattern forms a 2D photonic crystal with a lattice defect [36, 37]. Specifically, it is a photonic TCI of the Wu-Hu type [26, 33, 46], containing a disclination that hosts topological disclination states [14, 15, 37] to be used for waveguiding.

In the absence of the disclination, the cross-sectional structure has a  $C_{6v}$  point group symmetry, with each unit cell containing two air holes of (upper plot of Fig. 1b). We introduce a disclination of Frank angle  $-\pi/3$  into the lattice using a “cut-and-glue” process [13, 47] (see Extended Data Fig. 1a,b and Methods). This yields the five-fold rotationally symmetric structure of Fig. 1a, in which the hole radii are  $R_1 = 0.57d$  and  $R_2 = 0.35d$ , where  $d$  is the nearest-neighbour center-to-center distance in the original periodic lattice.

By design, such a structure is compatible with the stack-and-draw process [2, 3] for

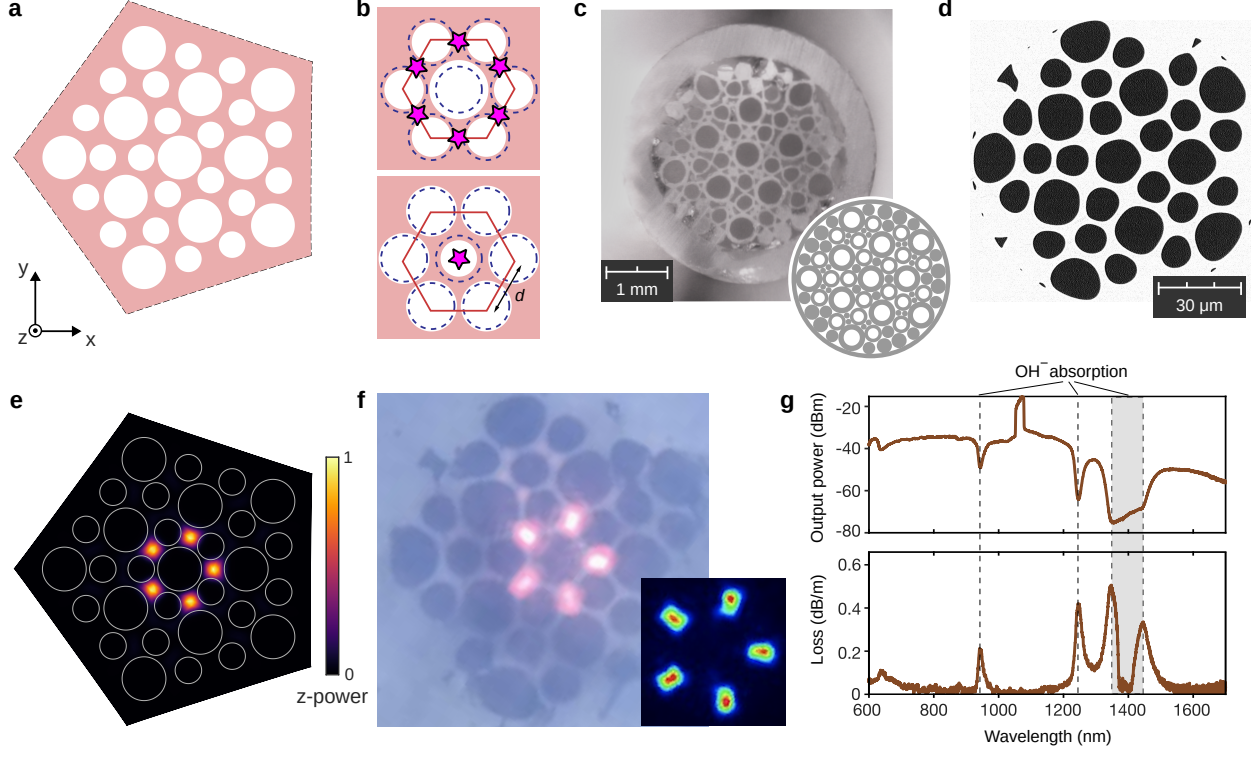


**FIG. 1. Topological photonic crystal fibre (TPCF) implementation.** **a**, Schematic of cross sectional photonic structure, comprising a topological crystalline insulator (TCI) with a disclination. **b**, Unit cell (red lines) for the disclination-free TCI, which has  $C_{6v}$  symmetry. Starting from a triangular lattice of equal air holes (dashed circles), the hole radii are alternately increased and decreased. For two different choices of modulation, the Wannier centers (magenta stars) are located at the unit cell's sides (upper plot) or center (lower plot). **c**, Photograph of the drawn fibre cane. Inset: stacking arrangement of the preform. **d**, Scanning electron microscope image of the TPCF's end face. **e**, Calculated intensity profile (power flow in the  $z$  direction) for a disclination state of the structure from **a** at  $k_z d / 2\pi = 2$ . The air holes are indicated by white circles. **f**, Optical microscope photograph of a 100 m TPCF, with a supercontinuum light source at the opposite end. Inset: infrared camera image of the same. **g**, Measured output power spectrum (upper plot) and transmission loss (lower plot) for a 52 m TPCF, using the same source.

fabricating PCFs. The air holes are formed from glass capillaries of two different radii, stacked within a glass jacket with major gaps filled by additional solid glass rods, as shown in the inset of Fig. 1c. This stacking arrangement is derived from the configuration of Fig. 1a by a jam-packing procedure (see Extended Data Fig. 1c, d and Methods). The preform is

drawn into a fibre cane (Fig. 1c), which is then further drawn into a fibre of diameter  $310\text{ }\mu\text{m}$  (see Methods). A scanning electron microscope image of the TPCF’s end face is shown in Fig. 1d. During the drawing process, most of the interstitial air holes are filled in, and the main air holes are slightly deformed (Extended Data Fig. 1e).

The key operating principle for the TPCF is that disclinations in TCIs can bind fractional spectral charges, giving rise to localised disclination states [14, 15, 37]. Such states are tied to the TCI topology via a bulk-defect correspondence, similar to the bulk-boundary correspondence governing topological corner states in disclination-free TCIs [12, 13] (in some circumstances, disclination states can even act as probes for band topological features that boundary probes cannot pick up). Whereas previous experimental realisations of topological disclination states [14, 15] have been based on structures that map closely to theoretical tight-binding models, our TPCF, like other photonic crystals, has no direct tight-binding analogue. Nonetheless, its photonic bandstructure can be shown to have nontrivial topology giving rise to disclination states. The Wannier centers are located on the sides of the periodic structure’s unit cell, as shown in the upper plot of Fig. 1b, implying that adding a disclination binds fractional charge [12, 14, 15]. Indeed, numerical simulations of Maxwell’s equations on the structure of Fig. 1a (see Methods) reveal the existence of guided modes that are strongly localised to the center of the sample (Fig. 1e). We will further investigate these disclination states, and their relationship to TCI topology, in Section 2. By contrast, reversing the large and small air holes yields a structure with trivial TCI topology, for which the Wannier centers lie at the centers of the unit cells (lower plot of Fig. 1b); we then find that introducing a disclination induces neither charge fractionalisation nor defect states (Extended Data Fig. 2d–h).

When light is coupled into the fabricated TPCF, we observe a spatially localised output profile at the end face (Fig. 1f). These optical microscope and infrared camera images are taken for a 100 m long TPCF with a supercontinuum laser source coupled to the opposite end (for details of the experimental setup, see Methods). The light is concentrated at five high-index (glass) regions placed symmetrically around the central air hole, closely matching the prediction of Fig. 1e.

The measured output spectrum shows that the TPCF can operate across a substantial wavelength band of around 700–1200 nm and 1500–1650 nm (Fig. 1g, upper plot). The spectral peak at 1060 nm is an inherent property of the supercontinuum source, while the

dips are due to hydroxyl ion absorption [48]. We determine the loss spectrum (Fig. 1g, lower plot) by comparing the outputs for TPCFs of length 67 m and 15 m, thus normalising away the source spectrum (see Methods). We find an average loss of around 10 dB/km over 1000–1200 nm and around 20 dB/km over 1530–1625 nm. Although we have not yet performed rigorous optimisation of the TPCF to minimise transmission losses, its current performance is already close to the level in commercial solid-core PCFs of similar core size (e.g., around 8 dB/km at 1064 nm for Thorlabs LMA-25, which has a core size of 25  $\mu\text{m}$ ).

## 2. GUIDED TOPOLOGICAL DEFECT MODES

Like most other PCFs, the TPCF, considered as a three-dimensional (3D) structure, lacks a complete photonic bandgap. We calculate the eigenmodes for the measured cross sectional structure of Fig. 1d (see Methods), and find a variety of transverse modes for each axial wavenumber  $k_z$  (Fig. 2a). There are numerous bulk modes (pink-shaded regions) and a small number of spatially-localised disclination states (red-and-blue lines), which we call guided topological defect modes (GTDMs). Over some ranges of  $k_z$  on the order of  $2\pi/d$ , there are gaps in the transverse spectrum, but the GTDMs do not lie within them. Although the bulk-defect correspondence predicts the disclination states, it does not require them to lie within a gap and there is no chiral-like symmetry pinning their frequencies [11, 44]. Absent fine-tuning, disclination states in previous models have shown a similar tendency to migrate into the bulk state continuum [14, 15].

The eigenmode calculations show a total of ten GTDMs. With increasing  $k_z$ , they dive below the “cladding light line” defined by the lowest-frequency bulk fibre modes. This feature is reminiscent of the “scalar limit” of guided modes in solid-core PCFs [6], and protects the GTDMs from coupling to bulk modes, similar to being in a bandgap. In the large  $k_z$  regime, the GTDMs become effectively degenerate in frequencies, as shown on the right side of Fig. 2a (for reference,  $20 \lesssim k_z d / 2\pi \lesssim 30$  corresponds to the 730–1100 nm operating regime of our experiments). They form two groups of five modes each, with one group having in-plane electric fields polarised in the radial direction, and the other being azimuthally polarised (Fig. 2b). The intensities are strongly localised to five high-index regions surrounding the central air hole, similar to the ideal case previously shown (Fig. 1e). The GTDMs also exhibit rising in-plane quality ( $Q$ ) factors and decreasing mode area with

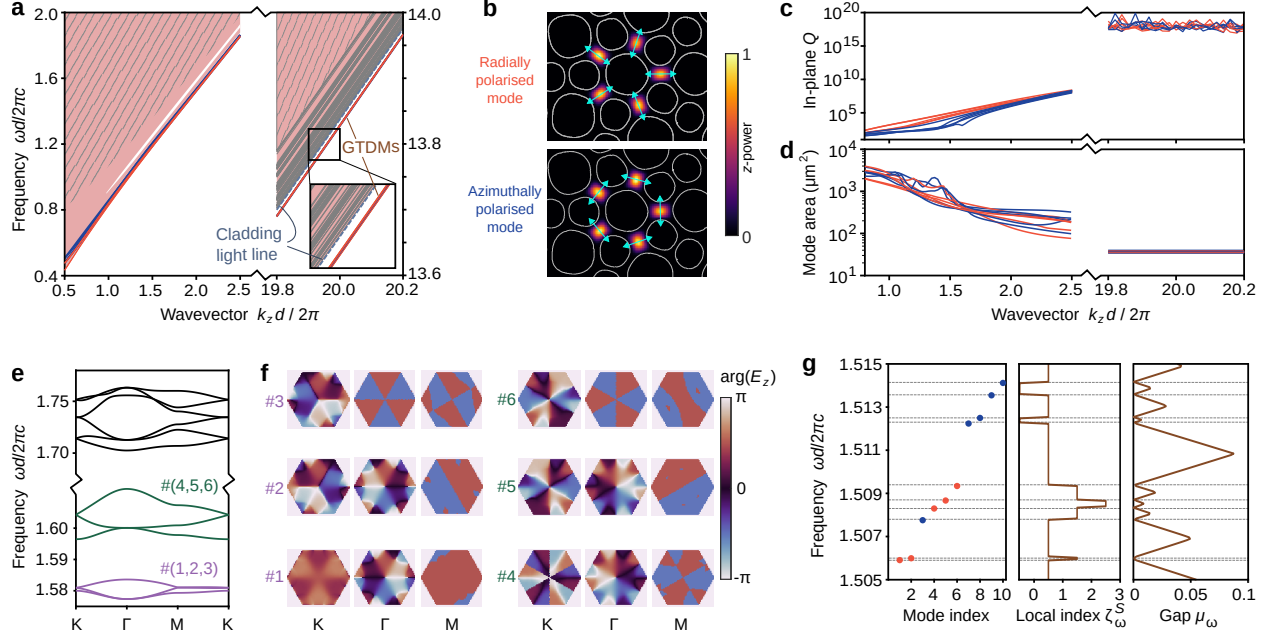


**FIG. 2. Analysis of guided topological defect modes (GTDMs).** **a**, Band diagram calculated from the measured structure in Fig. 1d (see Methods). The GTDMs are plotted in red (radially polarised) and blue (azimuthally polarised), and bulk state frequencies are drawn as pink areas; in the large- $k_z$  regime on the right side, dispersion curves for individual bulk states are plotted in gray. The gray-stroked region contains numerous modes that cannot be resolved numerically. **b**, Calculated intensity profiles (normalised power flow in  $z$ ) for exemplary radially and azimuthally polarised GTDMs at  $k_z d/2\pi = 20$ . Polarisation directions are indicated by cyan arrows. **c**, In-plane quality ( $Q$ ) factors of the GTDMs versus  $k_z$ . **d**, Mode areas of the GTDMs versus  $k_z$ . **e**, Band diagram for a periodic photonic structure at  $k_z d/2\pi = 2$ . **f**, Phase profiles of the out-of-plane electric field ( $E_z$ ) for the six Bloch states marked in **e** at high-symmetry momentum points. **g**, Topological characterisation based on spectral localiser. Left panel: eigenfrequencies of a symmetrised structure based on the preform profile. Center panel: the local index  $\zeta_\omega^S$ , where  $S$  is mirror symmetry around the  $x$  axis. Right panel: the local gap measure  $\mu_\omega$ . These results are calculated at  $k_z d/2\pi = 2$  (see Methods).

increasing  $k_z$  (Fig. 2c,d).

To understand the topological origins of the GTDMs, we turn to the underlying 2D TCI, which has circular air holes and is spatially periodic (upper plot of Fig. 1b). This has zero Chern number (even for  $k_z \neq 0$ ) and is thus Wannier representable [13]. In the bulk band



diagram for  $k_z d/2\pi = 2$  (Fig. 2e; for this low  $k_z$ , the bands are more easily distinguishable), we identify the two lowest sets of bands, denoted by  $\#(1, 2, 3)$  and  $\#(4, 5, 6)$ , which are separated from the others by gaps. From the phase profiles of the Bloch wavefunctions at high-symmetry momentum points (Fig. 2f), it can be seen that both sets of bands have symmetry indicators  $(\chi_M, \chi_K) = (2, 0)$  [12, 13, 15] (see Methods). Along with the aforementioned fact that the Wannier centers lie at the sides of the unit cell (Fig. 1b, upper plot), this implies that each set of bands binds fractional spectral charge, a necessary condition for localized topological states to emerge in this system [14]. We verify the charge fractionalisation with explicit calculations (see Extended Data Fig. 2 and Methods). Note that an analogous tight-binding model has five disclination states arising from three bands [15], so the existence of ten GTDMs can be interpreted as a doubling due to the polarisation degree of freedom. The above properties also hold at the larger  $k_z$  values where the TPCF operates.

To confirm that the GTDMs are topological modes, we employ an independent characterisation framework called the spectral localiser [16]. Unlike the methods in the previous paragraph, the spectral localiser directly analyses a real-space lattice, rather than the band-structure of a periodic precursor lattice. It yields (i) a local index  $\zeta_\omega^\mathcal{S}$  and (ii) a local gap measure  $\mu_\omega$ . The former allows us to classify the topology of the system, in terms of what kind of atomic limit it is continuable to, at each frequency  $\omega$  and subject to a specified symmetry  $\mathcal{S}$ . We take  $\mathcal{S}$  to be the global mirror symmetry  $y \rightarrow -y$  (note that the local  $C_{6v}$  symmetry of the precursor lattice is broken by the disclination); see Methods. Its value can be either integer or half-integer, but changes are quantized to integer values, corresponding to the number of topological states at frequency  $\omega$  [19]. Meanwhile,  $\mu_\omega$  quantifies the degree of topological protection: a topological state identified at  $\omega$  is guaranteed to be robust against perturbations  $\delta H$  for which  $\|\delta H\| < \mu_\omega$ , where  $\|\cdots\|$  denotes the largest singular value [20].

As shown in Fig. 2g, we find numerically that the 10 GTDMs are all associated with jumps in  $\zeta_\omega^\mathcal{S}$ , alongside nonzero  $\mu_\omega$  at intermediate frequencies, confirming that the GTDMs are robust topological modes. Moreover, after ascertaining the topological origin of the GTDMs, we employ a generalised local gap measure [60] to show quantitatively that the states are robust against fibre bends along arbitrary directions, including cases where the mirror symmetry  $\mathcal{S}$  is not preserved (see Extended Data Fig. 4 and Methods).

### 3. CHARACTERISATION OF FIBRE PROPERTIES

Having established the existence of GTDMs in TPCFs and their topological origins, we show that their properties are well-suited for waveguiding applications.

First, we verify that the theoretically-predicted features of the GTDMs, including their aforementioned degeneracy, polarisation, and spatial structure, are preserved during actual light transmission through the TPCF. Using the setup shown in Fig. 3a, we couple linearly polarised light at a single wavelength (1070 nm) into a 0.5 m long TPCF. By adjusting the position of the beam spot on the input face of the TPCF, we find that the intensity profile at the end face can be strongly concentrated onto each of the five high-index regions around the central air hole, an example of which is shown in the inset of Fig. 3a. This is consistent with the degeneracy structure of the GTDMs, which allows for a choice of basis functions that break the structure’s five-fold rotational symmetry and localise on each of the five symmetry axes. Next, we use a half-wave plate (HWP) to rotate the input polarisation angle, with another linear polariser at relative angle  $\theta_2$  placed at the end face (see Methods). As the HWP is rotated by 90 degrees (which causes the input polarisation to rotate by 180 degrees), the output intensity varies sinusoidally over one cycle, and this curve shifts by a half-cycle if  $\theta_2$  increases by 90 degrees (Fig. 3b). We then fix the HWP at an extremal intensity setting (vertical dashes in Fig. 3b) and measure the intensity along a radial line passing through the output spot (cyan dashes in the inset of Fig. 3a), obtaining the profile shown in Fig. 3c. We hence conclude that the polarisation of the GTDM is preserved as it passes through the TPCF. Moreover, by tuning the wavelength filter, we find that this property is relatively insensitive to the operating wavelength (Fig. 3d).

A guided mode in a PCF should also be robust against coupling to cladding modes (as those can in turn couple to free space). The GTDMs are advantageous in this respect, as they are tied to spectral charges originating from topological band invariants that do not change continuously when the system is weakly perturbed [9, 10]. The bulk-defect correspondence demands that this charge be localised to the disclination center, thereby obstructing mode delocalisation via the hybridisation of GTDMs with bulk states. This reasoning is also consistent with the nonzero local gap and index jump revealed by the spectral localiser (Extended Data Fig. 3). Although such “topological protection” is never absolute (e.g., it can be spoiled by finite-size effects), our TPCF evidently operates in a regime where the

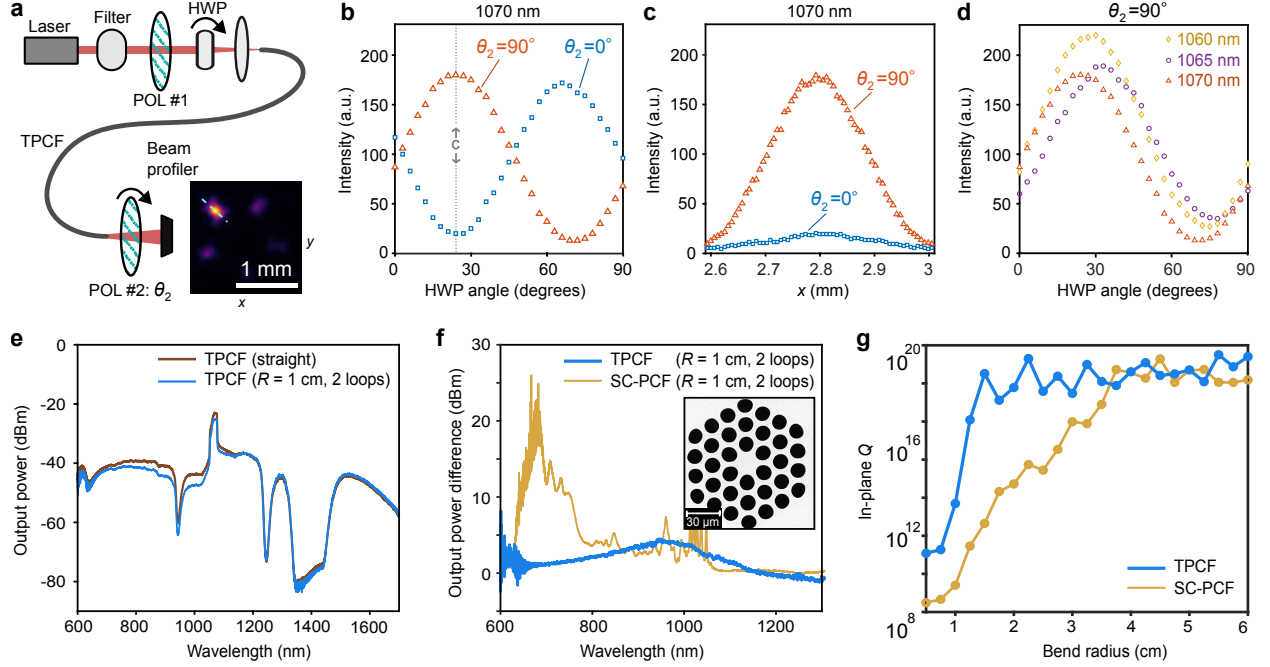


**FIG. 3. Polarisation dependence and bending resistance.** **a**, Experimental setup with a tunable filter, fixed linear polariser, and rotatable half-wave plate (HWP) between the source and the input face of a 0.5 m TPCF. A second linear polariser, with variable angle  $\theta_2$ , is placed between the end face and a beam profiler. Inset: a measured output intensity profile concentrated at one of the high-index regions around the central air hole. **b**, Measured intensity at the center of the selected spot, versus HWP angle. Results are shown for two values of  $\theta_2$  differing by  $90^\circ$ , with fixed wavelength 1070 nm. **c**, Variation of intensity with position, measured along a radial line passing through the selected spot (cyan dashes in the inset of **a**), with HWP fixed at  $24^\circ$  (vertical dashes in **b**). **d**, Intensity at the center of the selected spot versus HWP angle, for three different input wavelengths and fixed  $\theta_2 = 90^\circ$ . **e**, Output power spectrum for a straight TPCF (brown) and a TPCF with a two-loop bend of radius 1 cm (blue). **f**, Output power difference between a straight fibre and one with a two-loop bend of radius 1 cm, for the TPCF (blue) and a comparable solid-core (SC) PCF (yellow). Inset: Scanning electron microscope image of the SC-PCF. **g**, Calculated mean in-plane  $Q$  factors for the GTDMs in the TPCF (blue) and the fundamental core modes in the SC-PCF (yellow), for different bending radii at  $k_z d/2\pi = 30$  (corresponding to  $\sim 740$  nm). For the SC-PCF in **f**, **g**, the ratio between the air hole radii and the pitch is 0.38.

GTDMs indeed couple very weakly to other modes, as seen in the sizable gap between their dispersion relation and the cladding light line (Fig. 2a) and their strong spatial localisation (Fig. 1e).

Accordingly, we expect the TPCF to perform well even when physically deformed. To test this, we subject a 175 m long TPCF to two-loop bend, with 1 cm bending radius. Over much of the operating wavelength range, we find that the output power is only slightly reduced relative to the straight TPCF (Fig. 3e).

For comparison, we fabricate a solid-core PCF with similar core size and an air hole radii/pitch ratio of 0.38 (Fig. 3f, inset). For each fibre type, we measure the difference in output power (in dBm) between the straight and bent fibre (again using a two-loop bend of radius 1 cm). The solid-core PCF is found to have much stronger bending losses, by up to 25 dBm, particularly in the 600–800 nm range (Fig. 3f). To help understand these results, we perform numerical simulations in which the bend is modeled with a conformal transformation of the refractive index profile (see Methods). For the TPCF, the calculated  $Q$  factors for the GTDMs remain almost the same with decreasing bending radius, down to a radius of around 2 cm; by contrast, the solid-core PCF mode’s  $Q$  declines quickly as the bending radius goes below 4 cm (Fig. 3g).

#### 4. CONCLUSION AND OUTLOOK

We have realised a topological photonic crystal fibre (TPCF) supporting efficient broadband transmission that is robust under strong bending. The design is based on a topological crystalline insulator hosting localised disclination states due to a bulk-defect correspondence. Such a phenomenon has never previously been implemented in optical fibres, despite having been studied in the context of photonic crystal slabs [14, 15, 37]. The topological modes turn out to have specific features that are advantageous for fibre waveguiding. In particular, the fact that they can exist outside bandgaps, previously regarded as a relatively obscure quirk [14, 15], now enables the guided modes to reside below the cladding light line and thus decouple from the bulk modes. We have presented experimental results indicating that the TPCF is more robust to bending losses than a comparable solid-core PCF based on a conventional design. This calls for further quantitative studies, including comparisons to other fibre types as well as optimisations to our TPCF design, to determine whether topological

modes are indeed advantageous for optical fibres. It would also be interesting to explore alternative TPCF structures, including those employing different kinds of band topology; many of the frameworks we have used to analyse our TPCF, especially the spectral localiser, may be useful for guiding such work.

The built-in degeneracy of the topological modes in our TPCF offers particularly intriguing possibilities for further research. In the future, it should be possible to develop more optimised procedures for selectively addressing the ten degenerate topological modes, for the purposes of spatial division multiplexing [49], or studying their interaction with nonlinear effects in fibres [24]. It may also be possible to perform braiding on the degenerate topological modes, which would allow information to be encoded in their associated holonomy [50].

While this manuscript was in submission, we noticed a work demonstrating topological states in a helically twisted fiber [51]. Unlike the disclination states utilized in this work, those topological states are edge states circulating around the boundary of the fiber core [52].

We are grateful to Guoqing Chang for helpful discussions. This work was supported by the Singapore National Research Foundation (NRF) under Competitive Research Program (CRP) Nos. NRF-CRP23-2019-0005, NRF-CRP23-2019-0007, and NRF-CRP29-2022-0003, and the NRF Investigatorship NRF-NRFI08-2022-0001; the Singapore Ministry of Education Singapore (MOE-T2EP50122-0019); and by Singapore A\*STAR Grant No. A2090b0144. S. W. acknowledges support from the Laboratory Directed Research and Development program at Sandia National Laboratories. A. C. acknowledges support from the U.S. Department of Energy, Office of Basic Energy Sciences, Division of Materials Sciences and Engineering. This work was performed in part at the Center for Integrated Nanotechnologies, an Office of Science User Facility operated for the U.S. Department of Energy (DOE) Office of Science. Sandia National Laboratories is a multimission laboratory managed and operated by National Technology & Engineering Solutions of Sandia, LLC, a wholly owned subsidiary of Honeywell International, Inc., for the U. S. DOE's National Nuclear Security Administration under Contract No. DE-NA-0003525. The views expressed in the article do not necessarily represent the views of the U.S. DOE or the United States Government.

## METHODS

### A. Design and fabrication details

To design the TPCF structure, we begin with a wedge of opening angle  $\pi/3$  extracted from the periodic TCI structure (Extended Data Fig. 1a). This has circular air holes of alternating radii  $0.57d$  and  $0.35d$ , where  $d$  is the center-to-center distance between neighbouring holes. We deform this into a  $2\pi/5$  wedge by scaling each site’s azimuthal coordinate by  $6/5$  (Extended Data Fig. 1b). Copying this wedge to the remaining lattice sectors yields the structure of Fig. 1a, featuring a disclination of Frank angle  $-\pi/3$ .

Next we make small adjustments to the site positions, with the aim of improving the overall spatial uniformity of the PCF structure. This is achieved with the aid of a molecular dynamics (LAMMPS [53]) simulation, which moves a set of “atoms” centered at the site positions while also gradually enlarging their radii, subject to the fixed boundaries of the wedge [54]. This yields a jam-packed configuration (Extended Data Fig. 1c), in which the atomic radii ( $R'_1 = 0.65d$  and  $R'_2 = 0.43d$ ) correspond to the outer surfaces of the glass capillaries we aim to use in the fibre preform (see below). Finally, we define the air holes by downscaling the radii to  $R'_1 = 0.49d$  and  $R'_2 = 0.33d$ , corresponding to the inner surfaces of the capillaries. The resulting structure (Extended Data Fig. 1d) corresponds to the arrangement shown in the inset of Fig. 1c.

To fabricate the fibre, we draw glass tubes of outer (inner) diameter 25 mm (19 mm) into two sets of smaller tubes, or capillaries. After adjusting the drawing conditions (temperature, vacuum pressure, etc.), we obtain capillaries with outer diameters  $R'_1 = 3.33$  mm (11 pieces) and  $R'_2 = 2.18$  mm (20 pieces), close to the ideal ratio described above. Additional glass tubes of outer (inner) diameter 10 mm (3 mm), composed of the same silica material as the capillaries, are drawn into solid rods with collapsed inner air holes and outer diameters of 1.095 mm (5 pieces), 0.702 mm (20 pieces), 1.619 mm (15 pieces), and 1.905 mm (10 pieces). The capillaries and rods are stacked in a jacket of outer (inner) diameter 25 mm (19 mm) according to the arrangement in the inset of Fig. 1c, with the rods filling the major gaps between the capillaries. The preform is drawn into a preform cane of diameter 4.7 mm (Fig. 1d), which is in turn drawn into the TPCF in a fibre drawing tower.

The drawing process introduces deformations to the dielectric structure. From a scanning

electron microscope image of the fibre end face (Fig. 1d), we find that the holes become non-circular, but their positions are relatively unaffected (Extended Data Fig. 1e). Besides, the radii of air holes are slightly enlarged to  $R_1 = 0.55d$  and  $R_2 = 0.36d$ , which would be used in the preform hole profile for numerical simulations (see below). From numerical calculations of the eigenmodes (see below), we find that the deformations induce small shifts in the frequencies of the GTDMs and bulk states, but do not alter the qualitative features of the spectrum (Extended Data Fig. 1f,g).

We use the TPCF's measured hole profile (i.e., the black lines in Extended Data Fig. 1e) for most of our numerical calculations, including the band diagram (Fig. 2a) and various GTDM properties (Fig. 2b–d). The exceptions are the spectral charge calculation (Extended Data Fig. 2c) and bending performance calculation (Fig. 3g), which uses the preform hole profile, and the spectral localiser calculations (Fig. 2g and Extended Data Fig. 3b), which use the preform hole profile with a mirror symmetry-breaking perturbation (see below).

The conventional solid-core PCF is fabricated via the same stack-and-draw process, using a single set of glass tubes with outer (inner) radius 20 mm (16 mm) drawn into capillaries of outer diameter 2.28 mm (36 pieces). A single solid rod of 2.28 mm is used for the core. The hexagonal preform is supported in the cylindrical jacket by solid rods of outer diameter 0.61 mm (6 pieces), 0.75 mm (30 pieces) and 0.97 mm (12 pieces).

## B. Experimental setup

The optical fibres are illuminated using a supercontinuum laser (YSL Photonics SC-PRO 7 Supercontinuum Source, wavelength range 430–2400 nm, peak bandwidth 1050–1080 nm). The laser light passes through a lens and couples into the fibre head, which is fixed on a 3D stage. To optimise the input coupling, the fibre tail is connected to a power meter and the 3D stage is moved along three dimensions until the measured signal reaches a maximum. The power meter is then replaced by an optical signal analyser (Yokogawa AQ6370C, wavelength range 600–1700 nm) to record the output spectrum, or a camera beam profiler (Thorlabs BC106N-VIS/M, wavelength range 350–1100 nm) to record the mode profile.

To obtain the fibre loss spectrum (Fig. 1g), we follow a standard cut-and-measure procedure. The output spectrum is first measured for a TPCF of length 62 m. The fibre is then cut to a length of 15 m, and the output spectrum is measured again. The two spectra,

expressed in logarithmic units, are subtracted from each other and the result divided by the truncated length to give the loss spectrum.

When characterising the polarisation of the transmitted light (Fig. 3a–d), a tunable filter (Fianium LLTF Contrast SWIR, wavelength range 1000 nm–2300 nm) is placed right after the source. By adjusting the 3D stage on which the fibre head is mounted, we locate a setting in which the output intensity is concentrated on one of the five high-index regions (Fig. 3a, inset), and we then use this to obtain the results in Fig. 3b–d. The intensities are directly extracted from the beam profiler.

In the bending loss experiment (Fig. 3e–f), we place the fibre on a bending base with a preset bending radius. The other experimental procedures are as previously stated.

### C. Calculating photonic eigenmodes and band diagrams

An optical fibre is translationally symmetric in the axial ( $z$ ) direction. For a given axial wavenumber ( $k_z$ ), the electromagnetic eigenmodes can be determined by solving Maxwell’s equations in the 2D ( $x$ - $y$ ) plane. In this work, we perform the calculations numerically via the finite-element method (FEM) simulation software COMSOL Multiphysics, solving the full vectorial form of Maxwell’s equations with no additional approximations apart from the discretisation of space. The principal input to this calculation is the real-valued dielectric profile  $\epsilon(\mathbf{r})$ , where  $\mathbf{r} = (x, y)$  is the position in the 2D plane. We model the structure’s high-index (silica) and low-index (air) regions with  $\epsilon = 2.1$  and  $\epsilon = 1$  respectively.

Each calculated eigenmode  $\mu$  has some angular frequency  $\omega_\mu$  and electric field profile

$$\mathbf{E}_\mu(\mathbf{r}) \equiv \langle \mathbf{r} | \mu \rangle, \quad (1)$$

which is a complex 3-vector-valued field defined in the 2D space; from this, the full physical electric field is given by  $\text{Re}[\mathbf{E}_\mu(\mathbf{r}) \exp(ik_z z)]$ . Both  $\omega_\mu$  and  $\mathbf{E}_\mu(\mathbf{r})$  depend implicitly on  $k_z$ . The inner product between two normalised eigenmodes is defined as [21]

$$\langle \mu | \nu \rangle = \int d^2r \, \epsilon(\mathbf{r}) \, \mathbf{E}_\mu^*(\mathbf{r}) \cdot \mathbf{E}_\nu(\mathbf{r}). \quad (2)$$

If the boundary conditions are Hermitian (e.g., Dirichlet or periodic boundary conditions), Maxwell’s equations constitute a Hermitian generalised eigenproblem, so the orthogonality relation  $\langle \mu | \nu \rangle = \delta_{\mu\nu}$  holds [21].



When simulating the spatially finite TPCF structure, our choice of boundary conditions depends on the circumstances. For the spectral localiser (Fig. 2g and Extended Data Fig. 3b) and finding the spectral charges (Extended Data Fig. 2c), it is important that the eigenproblem be Hermitian, so we apply perfect electric conductor (PEC) boundary conditions to the system's exterior boundary. In all other cases, including calculations of the mode profiles (Fig. 1e and Fig. 2b) and dispersion relations (Fig. 2a), we apply impedance boundary conditions, which are equivalent to an infinite external medium of  $\epsilon = 2.1$ . Since light can leak out of the fibre and escape to infinity, the eigenfrequencies become complex; the real parts are used in the dispersion relations (Fig. 2a), and the imaginary parts are used to determine  $Q$  factors (Fig. 2c and Fig. 3g).

When analysing the underlying photonic crystal structure (Fig. 1b), which is spatially infinite and periodic in the  $x$ - $y$  plane, we impose Bloch's theorem by writing

$$\mathbf{E}_{n,\mathbf{k}}(\mathbf{r}) = \mathbf{u}_{n,\mathbf{k}}(\mathbf{r}) e^{i\mathbf{k}\cdot\mathbf{r}}, \quad (3)$$

where  $\mathbf{k}$  is a 2D wave-vector (quasimomentum) and  $n$  is a band index. Such eigenfunctions are calculated numerically using a single unit cell with Floquet-Bloch boundary conditions. The eigenproblem is Hermitian, with inner products between Bloch states given by

$$\langle n, \mathbf{k} | n', \mathbf{k}' \rangle = \int_{\text{u.c.}} d^2r \epsilon(\mathbf{r}) \mathbf{u}_{n,\mathbf{k}}^*(\mathbf{r}) \cdot \mathbf{u}_{n',\mathbf{k}'}(\mathbf{r}), \quad (4)$$

where the integral is taken over a single unit cell.

#### D. Wannier centers and spectral charge

To determine the Wannier centers of the photonic TCI (Fig. 1b), we use the Wilson loop approach [55, 56]. Given a set of degenerate bands  $n = 1, \dots, N$ , and a path  $k+l \leftarrow k$  passing across the Brillouin zone, we discretise the path into steps separated by  $\Delta\mathbf{k}$  and calculate

$$W_{k+l \leftarrow k} = G^{k+l-\Delta k} G^{k+l-2\Delta k} \dots G^{k+\Delta k} G^k \quad (5)$$

$$G_{mn}^k = \langle m, \mathbf{k} | n, (\mathbf{k} + \Delta\mathbf{k}) \rangle, \quad (6)$$

where Eq. (6) uses the inner product defined in Eq. (4). The eigenvalue spectrum of the  $W$  operator is adiabatically deformable to a set of centers of localised Wannier functions in real space. As established in previous works [56–58], topologically nontrivial TCIs have nonzero

values of the Berry phase  $\text{Im} \{ \log [\det (W_{k+l \leftarrow k})] \}$ , corresponding to the Wannier centers not being located at the center of the unit cell.

To construct the path of the Wilson loop, we first consider a rhombus with corners at four adjacent  $\Gamma$  points in the extended Brillouin zone (Extended Data Fig. 2a). The initial  $k$ -point is swept along the path  $\Gamma \rightarrow \text{M} \rightarrow \Gamma'$ , with the Wilson loop path taken parallel to the line  $\Gamma \rightarrow \Gamma''$ . As the initial  $k$ -point is varied, we observe nontrivial Berry phases remaining around  $\pm\pi$  (Extended Data Fig. 2b), corresponding to having Wannier centers localised to the Wyckoff position 3c [56].

Similar to other TCIs [12, 13, 15], our  $C_6$ -symmetric photonic structure's band topology can be characterised using symmetry indicators. Given a set of bands that are well-defined (i.e., not overlapping with any other bands), one defines  $\#\Pi_p^{(n)}$  as the number of bands at a high-symmetry momentum point  $\Pi \in \{\Gamma, \text{M}, \text{K}\}$  that has the  $C_n$  rotation eigenvalue  $e^{i2\pi(p-1)/n}$  ( $p = 1, \dots, n$ ). We can then calculate the topological index  $(\chi_{\text{M}}, \chi_{\text{K}})$ , where  $\chi_{\text{M}} = \#\text{M}_1^{(2)} - \#\Gamma_1^{(2)}$  and  $\chi_{\text{K}} = \#\text{K}_1^{(3)} - \#\Gamma_1^{(3)}$  [12]. From their Bloch function phase profiles (Fig. 2f), we see that bands  $\#(1, 2, 3)$  ( $\#(4, 5, 6)$ ) have

$$\begin{aligned} \#\Gamma_1^{(2)} &= 0(0), & \#\Gamma_1^{(3)} &= 1(1) \\ \#\text{M}_1^{(2)} &= 2(2) & \#\text{K}_1^{(3)} &= 1(1). \end{aligned} \tag{7}$$

Hence, both sets of bands have index  $(\chi_{\text{M}}, \chi_{\text{K}}) = (2, 0)$ .

The topological bulk-defect correspondence in such TCIs states that the symmetry indicators are related to defect charges of [13, 15]

$$Q_{\text{dis}} = \frac{\Omega}{2\pi} \left( \frac{3}{2} \chi_{\text{M}} - \chi_{\text{K}} \right) \bmod 1, \tag{8}$$

where  $\Omega = -\pi/3$  is the Frank angle of the disclination. Applying this to our TCI, the two sets of bands,  $\#(1, 2, 3)$  and  $\#(4, 5, 6)$ , are each predicted to produce fractional charge  $Q_{\text{dis}} = 1/2 \pmod{1}$ .

To verify the correspondence, we explicitly calculate the spectral charges. Even though there are two half-charges, we can distinguish them by exploiting the polarisation structure of the GTDMs. For each polarisation (radial or azimuthal), we pick out the five GTDMs and calculate

$$\sum_{u \in \text{GTDMs}} \int_S d^2r \, \epsilon(\mathbf{r}) \, |\mathbf{E}_\mu^*(\mathbf{r})|^2, \tag{9}$$

where  $S$  is one of the five unit cells surrounding the core unit cell. For each polarisation, we indeed find a charge of  $\approx 0.5$  in each of these five areas (Extended Data Fig. 2c). The calculation of spectral charge for the topological trivial case (Extended Data Fig. 2h) is similar but the summation is done for all the 90 bulk states below the bandgap, which are contributed from the lowest three bulk bands, i.e., band  $\#(1,2,3)$  in Extended Data Fig. 2d, of all the 30 intact unit cells.

### E. Spectral localiser

The calculations in the previous section strongly indicate that the TPCF should host topological disclination states, but there are some limitations in the argument. First, those characterisation frameworks refer to an underlying periodic bulk TCI, yet the symmetries on which the TCI relies are broken by the disclination and the various aforementioned deformations in the TPCF. Second, in a lattice exhibiting charge fractionalisation, it is sometimes possible for a strong lattice disturbance, like the core of a disclination, to remove the topological states expected to accompany the fractionalisation [14]. Finally, even if the lattice hosts topological disclination states, a given disclination state can still be accidental, i.e., non-topological. To resolve these doubts, we turn to the spectral localiser framework [16–19], which provides a way to directly establish that the disclination states in the TPCF are topological in origin as well as robust.

For a system with a single relevant position operator  $Y_c$ , the spectral localiser characterises the local topology at frequency  $\omega$  and position  $y$  by combining  $Y_c$  and the system’s Hamiltonian  $H_{\text{eff},c}(\omega)$  into

$$L_{(y,\omega)}(Y_c, H_{\text{eff},c}) = \begin{pmatrix} 0 & H_{\text{eff},c}(\omega) - i\kappa(Y_c - y\mathbf{1}_c) \\ H_{\text{eff},c}(\omega) + i\kappa(Y_c - y\mathbf{1}_c) & 0 \end{pmatrix}, \quad (10)$$

where  $\kappa$  is a scaling coefficient used to make the units consistent and to balance the spectral weight between  $Y_c$  and  $H_{\text{eff},c}$ . The notation here follows Ref. [43]. Both  $Y_c$  and  $H_{\text{eff},c}$  are numerically extracted from the discretised master equations in the FEM eigenfrequency solver—the same solver used all in our other numerical calculations. In particular,  $H_{\text{eff},c}$  is a matrix-valued function of the frequency  $\omega$ , meaning the photonic eigenmodes correspond to eigenvectors of  $H_{\text{eff},c}(\omega)$  with zero eigenvalue [43].

The TPCF structure possesses a mirror symmetry  $M_y : y \rightarrow -y$ , which satisfies  $M_y^2 = \mathbf{1}$ ,  $H_{\text{eff},c}M_y = M_yH_{\text{eff},c}$  and  $Y_cM_y = -M_yY_c$ . Using this symmetry, the reduced spectral localizer can be constructed as

$$L_\omega^{M_y}(Y_c, H_{\text{eff},c}) = [H_{\text{eff},c}(\omega) + i\kappa Y_c]M_y. \quad (11)$$

Topological defect modes can then be characterised by a local marker defined as

$$\zeta_\omega^{M_y}(Y_c, H_{\text{eff},c}) = \frac{1}{2} \text{sig} [L_\omega^{M_y}(Y_c, H_{\text{eff},c})], \quad (12)$$

where  $\text{sig}[\dots]$  denotes the signature (i.e., the difference between the total number of positive and negative eigenvalues). Note that Eq. (11) is Hermitian, so its signature is well-defined. If the value of Eq. (12) changes at a frequency  $\omega$ , it implies that the modes at that frequency have non-trivial topology [18]. Such a change happens when an eigenvalue of the spectral localiser crosses zero. Therefore, the local marker is also associated with a local measure of topological robustness via a “local gap”,

$$\mu_\omega(Y_c, H_{\text{eff},c}) = \min |\text{spec} [L_\omega^{M_y}(Y_c, H_{\text{eff},c})]|, \quad (13)$$

where  $\text{spec}[\dots]$  denotes the spectrum of the matrix.

When incorporating FEM matrices into the spectral localiser, there are two important subtleties to handle. The first involves the boundary conditions encoded into the FEM matrices. The subscript  $c$  in  $H_{\text{eff},c}$ ,  $Y_c$  and  $\mathbf{1}_c$  refers to “eliminated matrices”, which have undergone a procedure whereby all degrees of freedom involved in the boundary conditions are removed [43]. This projection is realised using matrices denoted by “Nullf” and “Null”, composed of basis vectors spanning the null space of the constraint force Jacobian matrix and the constraint Jacobian matrix, respectively: specifically,  $H_{\text{eff},c} = \text{Nullf}^T H_{\text{eff}} \text{Null}$ ,  $Y_c = \text{Nullf}^T Y \text{Null}$  and  $\mathbf{1}_c = \text{Nullf}^T \text{Null}$ , where  $H_{\text{eff}}$  and  $Y$  are matrices retrieved directly from the FEM (including boundary degrees of freedom).

The next subtlety involves the mirror symmetry. Even if the structure and the mesh are both symmetric with respect to  $M_y$ , the discretised FEM master equations may not yield a (non-eliminated) effective Hamiltonian  $H_{\text{eff}}$  commuting with  $M_y$ . This can be problematic since, as explained above, the local marker assumes mirror symmetry, which is necessary to guarantee the Hermiticity of Eq. (11). To bypass this difficulty, we decompose  $H_{\text{eff}}$  into even

and odd subspaces with respect to  $M_y$ ,

$$H_{\text{eff}} = \begin{pmatrix} H_{\text{eff},+} & 0 \\ 0 & H_{\text{eff},-} \end{pmatrix}. \quad (14)$$

The sub-Hamiltonians  $H_{\text{eff},+}$  and  $H_{\text{eff},-}$  are obtained from the FEM solver by applying symmetric/antisymmetric boundary conditions to the mirror line. In a similar way, we decompose the Nullf and Null matrices. In this basis, the mirror symmetry matrix reads

$$M_y = \begin{pmatrix} \mathbf{1}_+ & 0 \\ 0 & -\mathbf{1}_- \end{pmatrix}, \quad (15)$$

where  $\mathbf{1}_{\pm}$  are identity matrices of the same size as  $H_{\text{eff},\pm}$ . Finally, as the position operator  $Y$  anticommutes with  $M_y$ , we can write it as

$$Y = \begin{pmatrix} 0 & Y_- \\ Y_+ & 0 \end{pmatrix}, \quad (16)$$

where  $Y_+$  and  $Y_-$  are diagonal matrices constructed from the  $y$  coordinates of the symmetric and antisymmetric reduced systems.

We calculate the spectral localiser for a structure based on the ideal TPCF preform hole profile (Extended Data Fig. 1e), which is mirror symmetric with respect to the  $x$  axis. To aid the analysis, a mirror-symmetric refractive index perturbation is introduced to break the degeneracy between the doublet states among the GTDMs; we opt for a perturbation consistent with fibre bending (described in the next section). In Fig. 2g and Extended Data Fig. 3, we use a bending radius of  $R = 1.5$  cm, along with  $y = 0$  and  $\kappa = \kappa_0 [10^{-4} \|H_{\text{eff},c}(\omega_0)\| / \|Y_c\|]$ . The local gap is normalised by  $10^{-4} \|H_{\text{eff},c}(\omega_0)\|$ , where  $\|\cdots\|$  is the spectral norm (i.e., largest singular value). Moreover, Fig. 2g uses  $\kappa_0 = 0.01$  and  $\omega_0 = 1.5(2\pi c/d)$ , while Extended Data Fig. 3 uses  $\kappa_0 = 0.1$  and  $\omega_0 = 20.73(2\pi c/d)$ .

The spectral localiser can also quantify how robust the GTDMs are to perturbations that do *not* obey the previously-assumed mirror symmetry. To accomplish this, we employ the 2D localiser [59, 60]

$$L_{x,y,\omega}(X_c, Y_c, H_{\text{eff},c}) = \begin{pmatrix} H_{\text{eff},c}(\omega) & \kappa(X_c - x\mathbf{1}_c) - i\kappa(Y_c - y\mathbf{1}_c) \\ \kappa(X_c - x\mathbf{1}_c) + i\kappa(Y_c - y\mathbf{1}_c) & -H_{\text{eff},c}^\dagger(\omega) \end{pmatrix}. \quad (17)$$

Unlike the 1D localizer in Eq. (11), this can probe 2D positions  $(x, y)$  without assuming the structure to be mirror symmetric or the system's Hamiltonian to be Hermitian. We do not use this to formulate a local index, instead focusing on the local gap measure (also called a “radial local gap”) [60],

$$\mu_{x,y,\omega}(X_c, Y_c, H_{\text{eff},c}) = \sigma_{\min} [L_{x,y,\omega}(X_c, Y_c, H_{\text{eff},c})]. \quad (18)$$

Here we use the notation of Ref. [43], with  $\sigma_{\min}$  denoting the minimal singular value of the matrix. The condition  $\mu_{x,y,\omega} \approx 0$  is associated with the existence of a localised state near  $(x, y)$  at frequency  $\omega$ . In Extended Data Fig. 4a, we indeed observe zeros at the locations of the GTDMs (here we take  $k_z d/2\pi = 30$ , for which the GTDMs are near-degenerate).

We can now determine whether these zeros remain at these positions, or move away, when the structure is deformed. In Extended Data Fig. 4b–c, we show  $\mu_{x,y,\omega}$  for deformed structures corresponding to bending the fibre in the  $x$  axis, with bending radii of 4 cm and 1.5 cm respectively. Unlike the earlier perturbation, these deformations do *not* respect the mirror symmetry  $M_y$ . We find that the zeros of  $\mu_{x,y,\omega}$  corresponding to the GTDMs remain at almost the same positions near the fibre core, confirming the robustness of the GTDMs with respect to fibre bending [20].

## F. Further details of numerical simulations

The effective mode area plotted in Fig. 2c is defined as [3],

$$A = \frac{\left( \int d^2r |E_\mu(\mathbf{r})|^2 \right)^2}{\int d^2r |E_\mu(\mathbf{r})|^4}, \quad (19)$$

where the eigenmode  $E_\mu(\mathbf{r})$  has been normalised using the inner product Eq. (2).

To model the effects of bending the fibre (Fig. 3g and Extended Data Fig. 4), we perform a conformal transformation on the refractive index profile [61]. The modified refractive index (the square root of the dielectric constant) is

$$n'(x, y) = n(x, y) \left( 1 - \frac{x}{R} \right), \quad (20)$$

where  $n(x, y)$  is the refractive index distribution for the straight fibre with ideal preform

hole profile (Extended Data Fig. 1e), and  $R$  is the bending radius.

- 
- [1] J. D. Joannopoulos, P. R. Villeneuve and S. Fan, Photonic crystals: putting a new twist on light, *Nature* **386**, 143 (1997).
  - [2] J. C. Knight, Photonic crystal fibres, *Nature* **424**, 847 (2003).
  - [3] C. Markos, J. C. Travers, A. Abdolvand, B. J. Eggleton and O. Bang, Hybrid photonic-crystal fiber, *Rev. Mod. Phys.* **89**, 045003 (2017).
  - [4] E. N. Fokoua, S. A. Richardson, G. T. Jasion and F. Poletti, Loss in hollow-core optical fibers: mechanisms, scaling rules, and limits, *Adv. Opt. Photonics* **15**, 1 (2023).
  - [5] B. S. Temelkuran, D. Hart, G. Benoit, J. D. Joannopoulos and Y. Fink, Wavelength-scalable hollow optical fibres with large photonic bandgaps for CO<sub>2</sub> laser transmission, *Nature* **420**, 650 (2002).
  - [6] T. A. Birks, J. C. Knight and P. St. J. Russell, Endlessly single-mode photonic crystal fiber, *Opt. Lett.* **22**, 961 (1997).
  - [7] C. M. Smith, N. Venkataraman, M. T. Gallagher, D. Müller, J. A. West, N. F. Borrelli, D. C. Allan and K. W. Koch, Low-loss hollow-core silica/air photonic bandgap fibre, *Nature* **424**, 657 (2003).
  - [8] F. Couny, F. Benabid, P. J. Roberts, P. S. Light, and M. G. Raymer, Generation and Photonic Guidance of Multi-Octave Optical-Frequency Combs, *Science* **318**, 1118 (2007).
  - [9] B. Qi, H. Chen, L. Ge, P. Berini, R. Ma, T. Ozawa, H. Price, A. Amo, N. Goldman, M. Hafezi, L. Lu, M. Rechtsman, D. Schuster, J. Simon, O. Zilberberg and I. Carusotto, Topological photonics, *Rev. Mod. Phys.* **91**, 015006 (2019).
  - [10] G. Tang, X. He, F. Shi, J. Liu, X. Chen and J. Dong, Topological photonic crystals: physics, designs, and applications, *Laser Photonics Rev.* **16**, 2100300 (2022).
  - [11] S. Vaidya, A. Ghorashi, T. Christensen, M. C. Rechtsman and W. A. Benalcazar, Topological phases of photonic crystals under crystalline symmetries, *Phys. Rev. B* **108**, 085116 (2023).
  - [12] W. A. Benalcazar, T. Li and T. L. Hughes, Quantization of fractional corner charge in  $C_n$ -symmetric higher-order topological crystalline insulators, *Phys. Rev. B* **99**, 245151 (2019).
  - [13] T. Li, P. Zhu, W. A. Benalcazar, and T. L. Hughes, Fractional disclination charge in two-dimensional  $C_n$ -symmetric topological crystalline insulators, *Phys. Rev. B* **101**, 115115 (2020).

- [14] C. W. Peterson, T. Li, W. Jiang, T. L. Hughes and G. Bahl, Trapped fractional charges at bulk defects in topological insulators, *Nature* **589**, 376 (2021).
- [15] Y. Liu, S. Leung, F. Li, Z. Lin, X. Tao, Y. Poo and J. Jiang, Bulk–disclination correspondence in topological crystalline insulators, *Nature* **589**, 381 (2021).
- [16] T. A. Loring,  $K$ -theory and pseudospectra for topological insulators, *Ann. Phys.* **356**, 383 (2015).
- [17] A. Cerjan and T. A. Loring, An operator-based approach to topological photonics, *Nanophotonics* **11**, 4765 (2022).
- [18] A. Cerjan, T. A. Loring and F. Vides, Quadratic pseudospectrum for identifying localized states, *J. Math. Phys.* **64**, 023501 (2023).
- [19] A. Cerjan, T. A. Loring and H. Schulz-Baldes, Local Markers for Crystalline Topology, *Phys. Rev. Lett.* **132**, 073803 (2024).
- [20] A. Cerjan and T. A. Loring, Classifying photonic topology using the spectral localizer and numerical  $K$ -theory, *APL Photonics* **9**, 111102 (2024).
- [21] J. D. Joannopoulos, S. G. Johnson, J. N. Winn and R. D. Meade, *Photonic crystals: molding the flow of light*, 2nd ed. (Princeton University Press, 2008).
- [22] S. Noda, K. Kitamura, T. Okino, D. Yasuda and Y. Tanaka, Photonic-Crystal Surface-Emitting Lasers: Review and Introduction of Modulated-Photonic Crystals, *IEEE J. Sel. Top. Quantum Electron* **23**, 6 (2017).
- [23] W. Liu, H. Ma, A. Walsh, Advance in photonic crystal solar cells, *Renew. Sustain. Energy Rev.* **116**, 6 (2019).
- [24] T. Sylvestre, E. Genier, A. N. Ghosh, P. Bowen, G. Genty, J. Troles, A. Mussot, A. C. Peacock, M. Klimczak, A. M. Heidt, J. C. Travers, O. Bang and J. M. Dudley, Recent advances in supercontinuum generation in specialty optical fibers [Invited], *J. Opt. Soc. Am. B* **38**, 12 (2021).
- [25] V. S. Chaudhary, D. Kumar, B. P. Pandey and S. Kumar, Advances in photonic crystal fiber-based sensor for detection of physical and biochemical parameters—A review, *IEEE Sens. J.* **23**, 1012 (2022).
- [26] S. Barik, H. Miyake, W. DeGottardi, E. Waks and M. Hafezi, Two-dimensionally confined topological edge states in photonic crystals, *New J. Phys.* **18**, 113013 (2016).
- [27] T. Ma and G. Shvets, All-Si valley-Hall photonic topological insulator, *New J. Phys.* **18**,

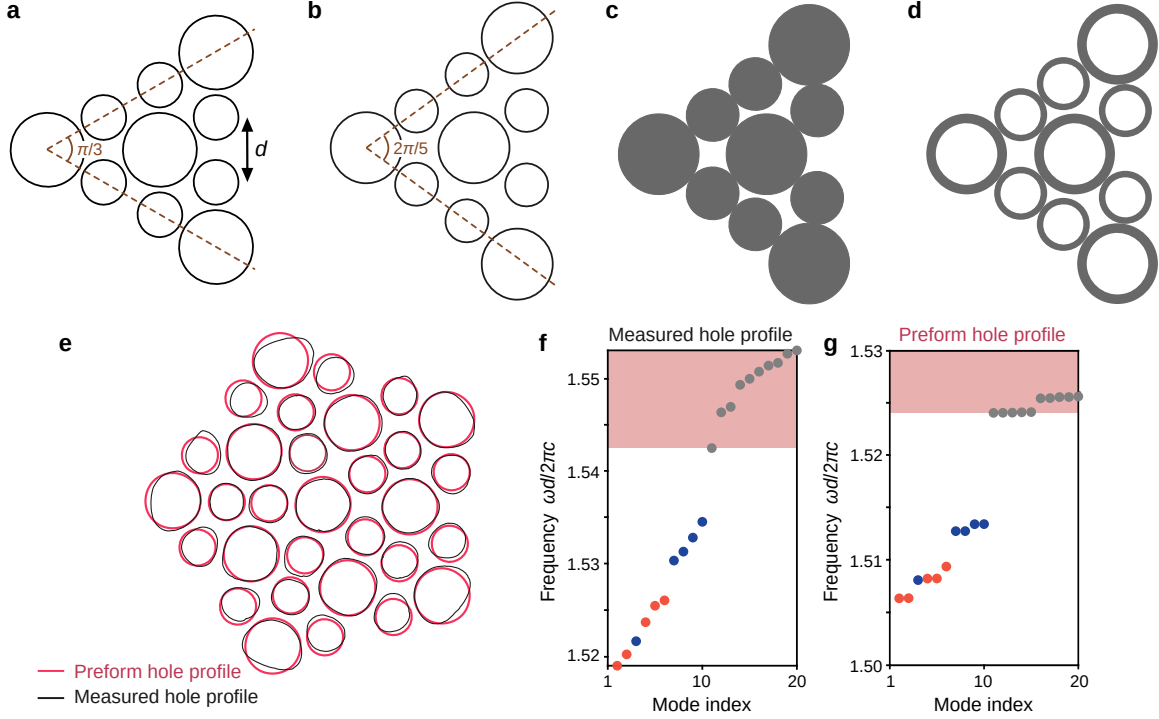


- 025012 (2016).
- [28] B. Bahari, A. Ndao, F. Vallini, A. E. Amili, Y. Fainman and B. Kanté, Nonreciprocal lasing in topological cavities of arbitrary geometries, *Science* **358**, 636 (2017).
  - [29] Y. Zeng, U. Chattopadhyay, B. Zhu, B. Qiang, J. Li, Y. Jin, L. Li, A. G. Davies, E. H. Linfield, B. Zhang, Y. D. Chong, and Q. J. Wang, Electrically pumped topological laser with valley edge modes, *Nature* **578**, 246 (2020).
  - [30] A. Dikopoltsev, T. H. Harder, E. Lustig, O. A. Egorov, J. Beierlein, A. Wolf, Y. Lumer, M. Emmerling, C. Schneider, S. Höfling, M. Segev, and S. Klemmt, Topological insulator vertical-cavity laser array, *Science* **373**, 1514 (2021).
  - [31] L. Piloizzi, D. Leykam, Z. Chen, and C. Conti, Topological photonic crystal fibers and ring resonators, *Opt. Lett.* **45**, 1415 (2020).
  - [32] M. Makwana, R. Wiltshaw, S. Guenneau, and R. Crasteri, Hybrid topological guiding mechanisms for photonic crystal fibers, *Opt. Express* **28**, 30871 (2020).
  - [33] H. Huang, Z. Ning, T. Kariyado, T. Amemiya, and X. Hu, Topological photonic crystal fiber with honeycomb structure, *Opt. Express* **31**, 27006 (2023).
  - [34] H. Lin, and L. Lu, Dirac-vortex topological photonic crystal fibre, *Light. Sci. Appl.* **9**, 202 (2020).
  - [35] N. Roberts, G. Baardink, J. Nunn, P. J. Mosley, and A. Souslov, Topological supermodes in photonic crystal fiber, *Sci. Adv.* **8**, eadd3522 (2022).
  - [36] N. D. Mermin, The topological theory of defects in ordered media, *Rev. Mod. Phys.* **51**, 591 (1979).
  - [37] Z. Lin, Q. Wang, Y. Liu, H. Xue, B. Zhang, Y. Chong and J. Jiang, Topological phenomena at defects in acoustic, photonic and solid-state lattices, *Nat. Rev. Phys.* **5**, 483 (2023).
  - [38] X. Gao, L. Yang, L. Hao, L. Zhang, J. Li, F. Bo, Z. Wang and L. Lu, Dirac-vortex topological cavities, *Nat. Nanotechn.* **15**, 1012 (2020).
  - [39] Q. Wang, H. Xue, B. Zhang and Y. D. Chong, Observation of protected photonic edge states induced by real-space topological lattice defects, *Phys. Rev. Lett.* **124**, 243602 (2020).
  - [40] L. Yang, G. Li, X. Gao and L. Lu, Topological-cavity surface-emitting laser, *Nat. Photon.* **16**, 279 (2022).
  - [41] S. Han, Y. Chua, Y. Zeng, B. Zhu, C. Wang, B. Qiang, Y. Jin, Q. Wang, L. Li, A. G. Davies, E. H. Linfield, Y. Chong, B. Zhang and Q. J. Wang, Photonic Majorana quantum cascade

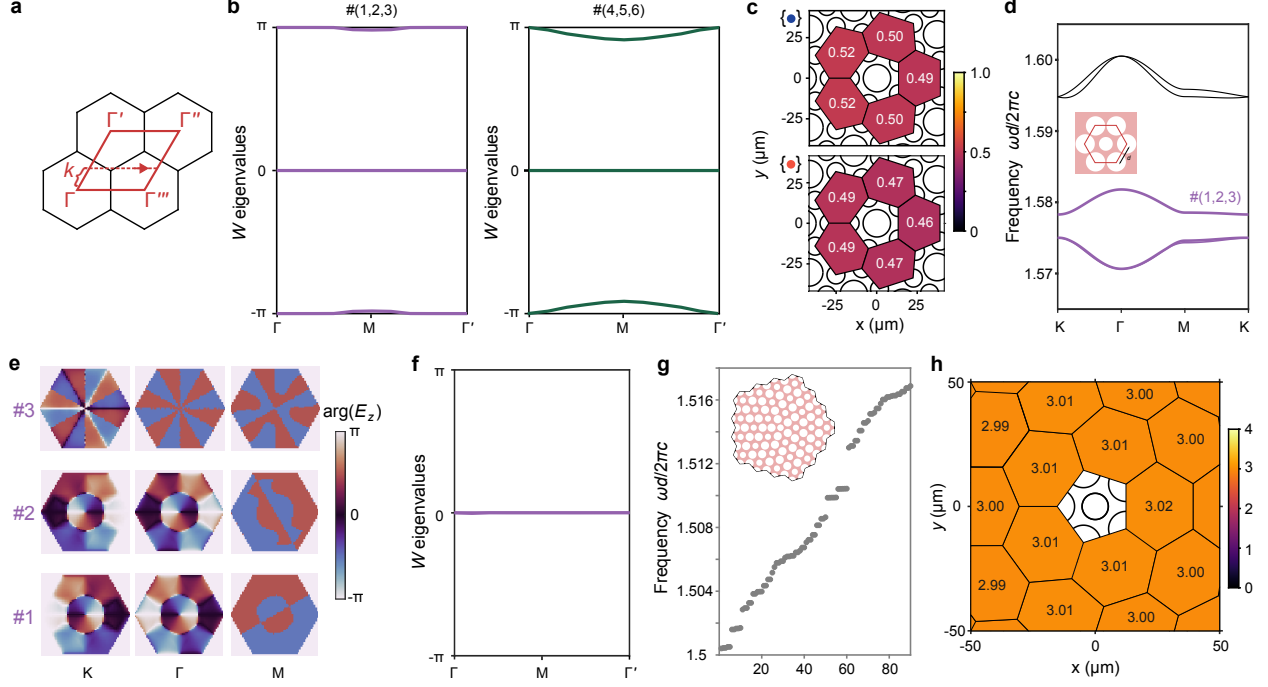
- laser with polarization-winding emission, *Nat. Commun.* **14**, 707 (2023).
- [42] M. Hwang, H. Kim, J. Kim, B. Yang, Y. Kivshar and H. Park, Vortex nanolaser based on a photonic disclination cavity, *Nat. Photon.* **18**, 286 (2024).
  - [43] S. Wong, T. A. Loring and A. Cerjan, Classifying topology in photonic crystal slabs with radiative environments, *npj. Nanophotonics* **1**, 19 (2024).
  - [44] J. Noh, T. Schuster, T. Iadecola, . Huang, M. Wang, K. P. Chen, C. Chamon and M. C. Rechtsman, Braiding photonic topological zero modes, *Nat. Phys.* **16**, 989 (2020).
  - [45] Q. Wang, Y. Ge, H. Sun, H. Xue, D. Jia, Y. Guan, S. Yuan, B. Zhang and Y. D. Chong, Vortex states in an acoustic Weyl crystal with a topological lattice defect, *Nat. Commun.* **12**, 1 (2021).
  - [46] L. H. Wu and X. Hu, Scheme for Achieving a Topological Photonic Crystal by Using Dielectric Material, *Phys. Rev. Lett.* **114**, 223901 (2015).
  - [47] P. M. Chaikin and T. C. Lubensky, *Principles of Condensed Matter Physics*, (Cambridge University, Cambridge, England, 2000).
  - [48] M. H. Weik, *Computer Science and Communications Dictionary*, hydroxyl ion absorption. (Springer US, 2017).
  - [49] R. G. H. van Uden, R. A. Correa, E. A. Lopez, F. M. Huijskens, C. Xia, G. Li, A. Schülzgen, H. de Waardt, A. M. J. Koonen and C. M. Okonkwo, Ultra-high-density spatial division multiplexing with a few-mode multicore fibre, *Nat. Photon.* **8**, 865 (2014).
  - [50] Z.-G. Chen, R.-Y. Zhang, C. T. Chan, and G. Ma, Classical non-Abelian braiding of acoustic modes, *Nat. Phys.* **18**, 179 (2022).
  - [51] R. Beravat, G. K. Wong, M. H. Frosz, X. M. Xi and P. St. J. Russell, Twist-induced guidance in coreless photonic crystal fiber: A helical channel for light, *Sci. Adv.* **2**, e1601421 (2016).
  - [52] N. Roberts, B. Salter, J. Binysh, P. J. Mosley and A. Souslov, Twisted fibre: a photonic topological insulator, *arXiv:2411.13064* (2024).
  - [53] A. P. Thompson, *et al.*, LAMMPS—a flexible simulation tool for particle-based materials modeling at the atomic, meso, and continuum scales, *Comp. Phys. Comm.* **271**, 10817 (2022).
  - [54] J.-K. Yang, C. Schreck, H. Noh, S.-F. Liew, M. I. Guy, C. S. O’Hern, and H. Cao, Photonic band-gap effects in two-dimensional polycrystalline and amorphous structures, *Phys. Rev. A* **82**, 053838 (2010).
  - [55] H. Wang, G. Guo and J. Jiang, Band topology in classical waves: Wilson-loop approach to

- topological numbers and fragile topology, *New J. Phys.* **21**, 093029 (2019).
- [56] M. Blanco de Paz, C. Devescovi, G. Giedke, J. J. Saenz, M. G. Vergniory, B. Bradlyn, D. Bercioux and A. García Etxarri, Tutorial: Computing topological invariants in 2D photonic crystals, *Adv. Quantum Technol.* **3**, 1900117 (2020).
  - [57] T. Neupert and F. Schindler, *Topological Matter*, pp. 31–61 (Springer International Publishing, 2018).
  - [58] D. Vanderbilt, *Berry Phases in Electronic Structure Theory: Electric Polarization, Orbital Magnetization and Topological Insulators*, (Cambridge University Press, 2018).
  - [59] A. Cerjan, L. Koekenbier, H. S. Baldes, Spectral localizer for line-gapped non-hermitian systems, *J. Math. Phys.* **64**, 082102 (2023).
  - [60] J. J. Garcia, A. Cerjan and T. A. Loring, Clifford and quadratic composite operators with applications to non-Hermitian physics, arXiv:2410.03880v1 (2024).
  - [61] F. Poletti, Nested antiresonant nodeless hollow core fiber, *Opt. Express* **22**, 23807 (2014).

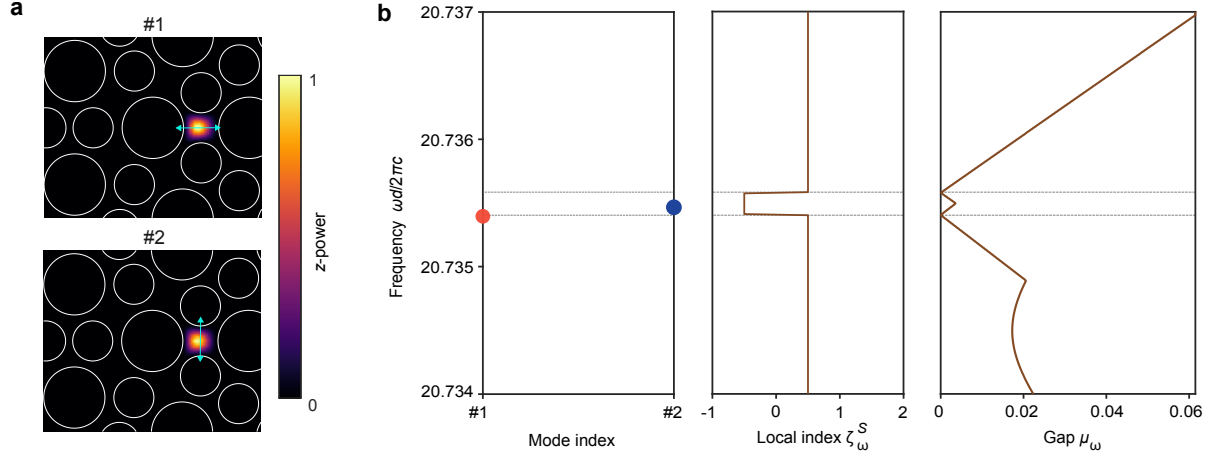
## 5. EXTENDED DATA FIGURES



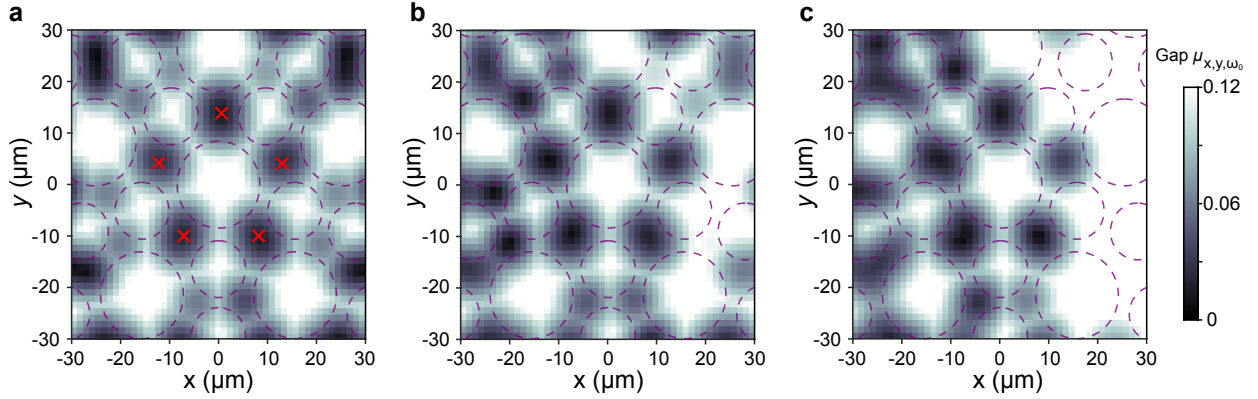
Extended Data Figure 1. **Lattice design.** **a**, Wedge with opening angle  $\pi/3$ , extracted from a triangular lattice with nearest neighbor center-to-center spacing  $d$ . The discs (air holes) have alternating radii of  $0.57d$  and  $0.35d$ . **b**, Wedge with opening angle  $2\pi/5$ , generated from **a** by uniformly scaling the azimuthal coordinates of the site centers. This corresponds to the structure shown in Fig. 1a. **c**, Wedge generated from **b** by gradually enlarging the disc radii and adjusting their positions, with boundaries fixed, until they are jam-packed. **d**, Structure generated from **c** by assigning inner air holes of radius  $R'_1 = 0.49d$  and  $R'_2 = 0.33d$  to the discs. This corresponds to the target stacking arrangement shown in Fig. 1c. **e**, Comparison between the preform hole profile based on **d** (black lines), and the measured hole profile of the fabricated TPCF (pink lines). The air holes radii are slightly enlarged to  $R_1 = 0.55d$  and  $R_2 = 0.36d$ . **f, g**, Calculated eigenfrequencies at  $k_z d/2\pi = 2$  for the measured hole profile (**f**) and the preform hole profile (**g**). Red (blue) data points correspond to GTDMs with radial (azimuthal) polarisation, while gray data points are bulk states. The pink-shaded region indicates the bulk band.



Extended Data Figure 2. **Wilson loop and spectral charge calculations.** **a**, Schematic of the Wilson loop. The initial  $k$ -point lies along the path  $\Gamma \rightarrow \Gamma'$ , and the Wilson loop follows the dashed line running parallel to  $\Gamma-\Gamma'''$ . **b**, Berry phases of the Wilson loop operator for different initial  $k$  points, using the bulk bands  $\#(1, 2, 3)$  (left panel) and  $\#(4, 5, 6)$  (right panel) in Fig.2e. **c**, Calculated spectral charges (white numbers) in the five unit cells surrounding the central unit cell, for azimuthally polarised GTDMs (upper panel) and radially polarized GTDMs (lower panel) in Fig.2g and Extended Data Fig.1g. **d**, Lowest five bands for the periodic photonic structure with trivial crystalline topology, calculated from the unit cell in Fig.1b (lower plot). **e**, Phase profiles of the out-of-plane electric field ( $E_z$ ) for the Bloch states  $\#(1, 2, 3)$  in the trivial structure of **d** at high-symmetry momentum points. **f**, Berry phases of the Wilson loop operator at different initial  $k$  for the trivial bulk bands  $\#(1, 2, 3)$ . **g**, Calculated eigenfrequencies for the trivial PCF structure, based on **c** but with large and small air holes switched. Inset: schematic of the lattice, composed of 30 intact unit cells and a central defect. **h**, Calculated spectral charges (black numbers) for the structure of **g**. In **b-g**, the eigenmodes are calculated at  $k_z d/2\pi = 2$ . The spectral charge calculations are performed using symmetric preform hole profiles.



Extended Data Figure 3. **Spectral localizer results for bent fibre.** **a**, Calculated intensity profiles (normalized power flow in  $z$ ) for a pair of radially and azimuthally polarised GTDMs. Polarisation directions are indicated by cyan arrows. **b**, Eigenmode spectrum (left panel), local index  $\zeta_\omega^S$  (center panel) and local gap  $\mu_\omega$  (right panel) from spectral localizer calculations. In these calculations, we use  $k_z d/2\pi = 30$  and bending radius  $R = 1.5$  cm.



Extended Data Figure 4. **Characterisation of GTDM robustness by local gap.** **a**, Local gap  $\mu_{x,y,\omega_0}$  calculated at  $k_z d/2\pi = 30$  and  $\omega_0 = 20.73(2\pi c/d)$  for an ideal preform hole profile, consisting of the structure of Extended Data Fig. 1e rotated counterclockwise by 90 degrees. The five zeros of  $\mu_{x,y,\omega_0}$  near the disclination core (red crosses) correspond to the GTDMs, previously identified as topological states via jumps in a local index (Fig. 2g). **b**, **c**, Local gaps calculated at the same  $k_z$  and  $\omega_0$  for structures deformed by bending the fibre along  $x$  with bending radius  $R = 4$  cm (**b**) and  $R = 1.5$  cm (**c**). This bending spoils the mirror symmetry previously assumed in the symmetry-reduced spectral localiser analysis.